

DEEP LEARNING-BASED PENETRATION DEPTH PREDICTION IN Al/Cu LASER WELDING USING SPECTROMETER SIGNAL AND CCD IMAGE

Paper #193

Sanghoon Kang^{1,2}, Minjung Kang¹, Yong Hoon Jang^{2,*}, Cheolhee Kim^{1,3,*}

¹ Joining R&D Group, Korea Institute of Industrial Technology, Incheon 21999, South Korea

² School of Mechanical Engineering, Yonsei University, South Korea 03722, South Korea

³ Department of Mechanical and Materials Engineering, Portland State University, OR 97207, USA

* Contact: chkim@kitech.re.kr, cheol@pdx.edu; jyh@yonsei.ac.kr

Abstract

In the laser welding of thin Al/Cu sheets, proper penetration depth and wide interface bead width ensure stable joint strength and low electrical conductance. In this study, we proposed deep learning models to predict the penetration depth. The inputs for the prediction models were 500 Hz-sampled low-cost charge-coupled device (CCD) camera images and 100 Hz-sampled spectral signals. The output was the penetration depth estimated from the keyhole depth measured coaxially using optical coherence tomography. A unisensor model using a CCD image and multisensor model using a CCD image and the spectrometer signal were proposed in this study. The input and output of the data points were resampled at 100 Hz and 500 Hz, respectively. The 500 Hz models showed better performance than the 100 Hz models, and the multisensor models more accurately predicted the penetration depth than the unisensor models. The most accurate model had a coefficient of determination (R^2) of 0.999985 and mean absolute error of 0.02035 mm in the model test. It was demonstrated that low-cost sensors can successfully predict the penetration depth during Al/Cu laser welding.

Introduction

Electric vehicles are gradually replacing conventional engine-based vehicles, and the importance of battery systems is increasing significantly in the automotive industry. Currently, lithium-ion batteries are the most commonly used automotive batteries, and aluminum and copper are employed as materials for electrodes, tabs, and bus bars to carry electric current [1]. Although dissimilar metal joining between Al and Cu is inevitable in battery manufacturing, its weldability is poor because of its high thermal conductivity, varying melting temperatures, high optical reflectivity, and brittle intermetallic compound (IMC) formation [2,3]. Laser welding and ultrasonic welding are industrially

preferred to mechanical joining or conventional fusion welding technologies, such as arc and resistance spot welding, for minimizing the thermal effects and IMC formation [1,4,5]. Ultrasonic welding is a solid-state welding process that can eliminate metallurgical defects in fusion welding processes; however, the characterization and monitoring of welding quality are relatively difficult compared with laser welding [6,7]. Moreover, laser welding has better electrical conductance [8,9] and productivity [1] than other welding processes. Failure at the welded joint can cause thermal runaway in automotive batteries [10,11], and the quality monitoring of laser welding is critical for manufacturers.

In overlap-welded Al/Cu joints, the weld penetration depth into the lower sheet must be precisely controlled to guarantee mechanical load and electrical current-carrying capacities because insufficient penetration depth reduces the joint area, and excessive penetration depth increases IMC formation [2,3,12]. Recently, deep learning models for penetration-depth prediction have been introduced for laser welding. In particular, laser welding for dissimilar material combinations of Al/Cu [13], various grades of steel [14], and Cu/stainless steel [15] have been investigated using neural network models in which the penetration depth was estimated from process parameters.

Efficient sensors and sufficient datasets are prerequisites for developing a deep learning model to predict in situ penetration depth. Coaxial high imaging has been suggested for monitoring keyhole behavior and penetration modes; however, its application is limited to full penetration [16]. The molten pool and keyhole behavior in laser welding were monitored using a charge-coupled device (CCD) camera; however, related studies on penetration depth prediction have not been introduced in Al/Cu dissimilar material joints. In comparison, photodiode-based monitoring showed excellent performance based on various optical

emissions of Al and Cu. The emission bands at 395 nm, 485 nm, and 580 nm were used to estimate the penetration mode into the lower sheet [17-20]; however, photodiode-based research has not been extended to the quantitative prediction of the penetration depth. In this study, a low-cost CCD camera and spectrometer with a wide spectrum range were chosen as the input sensors.

Welding penetration is usually measured in transverse and longitudinal cross-sections to collect more data from specimens [21]. However, the direct measurement of penetration depth from cross-sections has inherent limitations in increasing the number of datasets and synchronizing with other sensors. Recently, keyhole depth was measured using optical coherence tomography (OCT) [22,23], and a previous study proved that the OCT signal is well correlated with the penetration depth in Al/Cu laser welding [19]. The OCT signal was chosen as the output, indicating the penetration depth owing to a high sampling rate and easy synchronization with the input sensor signals.

In this study, convolutional neural network (CNN) models employed to predict the penetration depth were investigated. CCD images and spectrometer signals were recorded as input, and OCT signals were collected as the output. The input and output were resampled at 100 Hz and 500 Hz, respectively. The performances of the unisensor deep learning models based on CCD images and the multisensor deep learning models considering additional spectrometer signals were compared after training. The penetration depth prediction models were verified by an experiment with varying laser power, which showed that the developed models can accurately predict the penetration depth.

Experiments

The base metals were Al 1050-H alloy with a thickness of 0.4 mm and C1100-1/2H copper alloy with a thickness of 1.0 mm. The chemical composition of the Al alloy is listed in Table 1. The chemical composition of the Cu alloy was 99.95% Cu and less than 10 ppm oxygen. The ultimate tensile strengths of the Al and Cu alloys were 158 MPa and 268 MPa, respectively.

Table 1. Chemical composition of Al 1050 alloy (wt %)

Al	Si	Fe	Cu	Mn	Mg	Zn	Ti	V
99.59	0.068	0.286	0.003	0.001	0.001	0.002	0.023	0.016

The Al and Cu specimens were machined as sheets with dimensions of 50 mm and 150 mm in width and length, respectively; an Al sheet was fully overlapped onto a Cu sheet for welding. The weld length was 100 mm. A welding laser beam was generated using a fiber laser with a beam quality of 2 mm·mrad and maximum

power of 6 kW, and delivered to a laser welding head via an optical fiber with a diameter of 200 μm . The laser welding head consisted of focusing optics, illumination laser optics, OCT sensors, CCD cameras, and spectrometers (Fig. 1). The focal length of the focusing optics was 200 mm, and the laser beam was focused on the top surface of the upper specimens with a beam diameter of 270 μm . The illumination laser had a wavelength of 980 nm, and the specimens were irradiated with a power of 100 W and an angle of 40° from the horizontal line. The OCT sensor monitored keyhole depth at a sampling frequency of 135 kHz. Because the OCT sensor measured the keyhole depth, the relationship between the keyhole depth and penetration depth was calibrated to estimate the penetration as an output of the models. The CCD camera images were captured at a frame rate of 500 Hz after band-pass filtering at a 980 ± 5 nm wavelength. The spectrometer had a sensing wavelength range of 200–1100 nm, sampling rate of 100 Hz, and an optical resolution of 0.47 nm in full width at half maximum. The CCD camera and spectrometer sensor were connected to the laser head via a dichroic mirror.

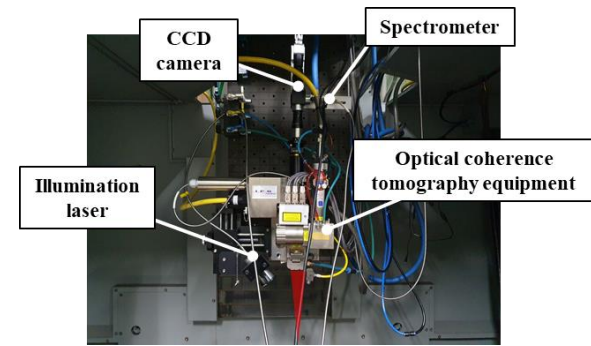


Fig 1. Laser head configuration

The welding speed was set from 3 m/min to 7 m/min in increments of 1 m/min, and five laser powers were selected to vary the weld penetration depth for a particular welding speed. At each welding speed, the lowest laser power was set to melt only the upper plate, and the laser power was increased to create a stable interface between the upper and lower plates. The details of the welding parameters are presented in Table 2.

Table 2. Welding parameters used in experiments

Laser power (W)	700–1600
Laser beam diameter (mm)	0.27
Focal length (mm)	200

The CCD images, OCT signal, and spectrometer signals were recorded at their own sampling rate, but in

synchronization. The signals, except 0.3 s of start and end of the welding, were used for modelling.

In the verification test, the laser output power was increased from 600 W to 900 W along a welding length of 100 mm at a fixed welding speed of 5 m/min. The verification specimen was cut longitudinally, and the penetration depth was measured and compared with the penetration depth estimated by the developed models.

Data preparation and Models

Penetration depth calibration

The weld penetration depth was estimated using OCT signals to measure the keyhole depth. The relationship between the penetration depth and OCT signals was calibrated by measuring two characteristics of the sample cases. The samples were prepared under 12 welding conditions, as shown in Fig. 2. The penetration depth was measured on the cross sections of the three samples extracted from each specimen. The OCT signals and penetration depths were averaged under each welding condition. The measured characteristics showed a linear relationship, with a coefficient of determination of 0.9304 (Fig. 3).

Data preprocessing

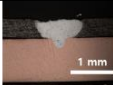
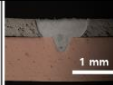
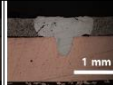
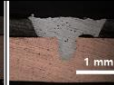
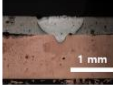
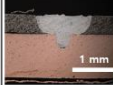
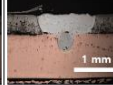
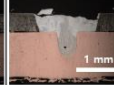
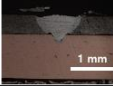
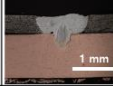
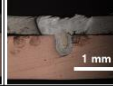
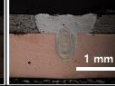
Welding speed (m/min)	3			
Laser power (W)	792	882	972	1062
Cross section				
Welding speed (m/min)	5			
Laser power (W)	877	1027	1177	1327
Cross section				
Welding speed (m/min)	7			
Laser power (W)	970	1180	1390	1600
Cross section				

Fig 2. Penetration depth measurement from cross-sections

Two input signals and one output signal had different sampling frequencies. The input and output signals were resampled at frequencies of 100 Hz and 500 Hz, respectively. After deep learning training, 100 Hz sampled data-based prediction models were compared

with 500 Hz resampled data-based prediction models. The details of resampling are presented below.

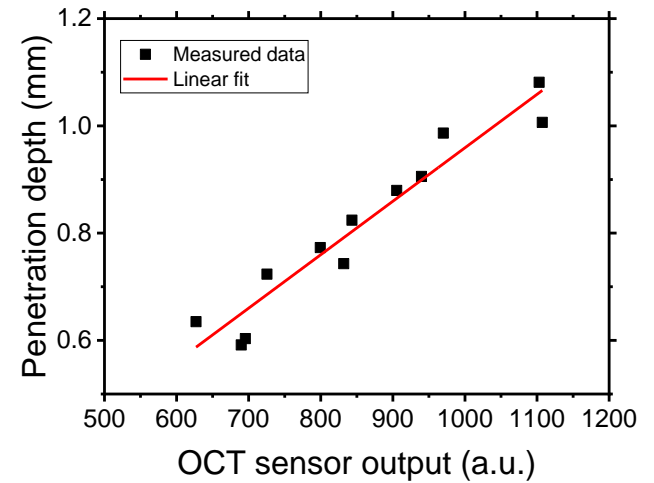


Fig 3. Relation between measured penetration depth and OCT signal

Coaxial images of the welds, including a keyhole, molten pool, and solidified weld bead, were recorded with a resolution of 242×472 pixels, and a sampling rate of 500 Hz. In the 500 Hz prediction models, as-received images were used as an input signal, and in the 100 Hz prediction models, the images were resampled by averaging every five images. As shown in Fig. 4, the averaged image shows a clear and continuous edge of objects and less noise, despite slight blurring.

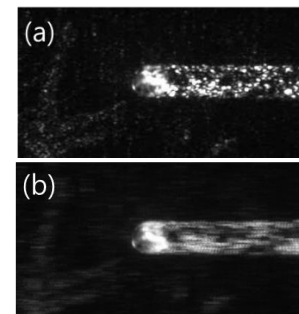


Fig. 4 Example of CCD images. (a) Raw image and (b) resampled image (100 Hz)

Spectrometer signals were collected at a sampling rate of 100 Hz, and used as inputs for the 100 Hz prediction models. In the 500 Hz predictions models, the raw spectrometer signal was up-sampled per wavelength using the Fourier method [24] (Fig. 5). In the spectrometer signal, relatively high peaks were observed by the reflection of the process laser (1070 nm), illumination laser (980 nm), and OCT reference laser (around 838 nm), as shown in Fig.6a, as well as

material emission signals, as shown in Fig. 6b. The wavelengths of the local peaks coincide with the copper emission wavelengths in the National Institute of Standards and Technology (NIST) database [25].

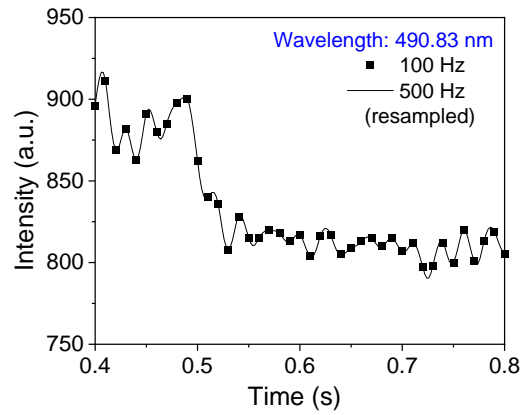
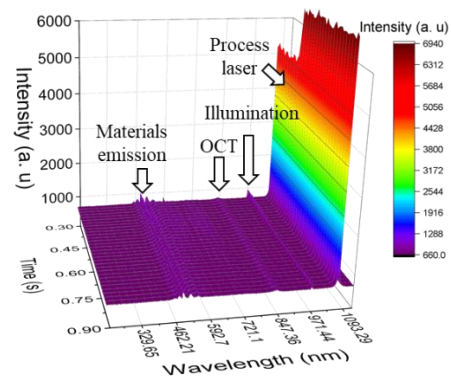
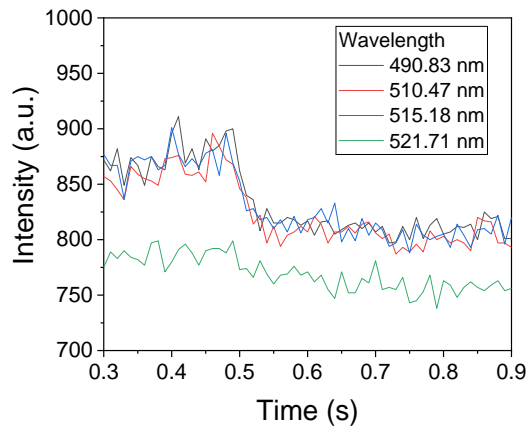


Fig. 5 Spectrometer signal and resampling at a wavelength of 490.83 nm



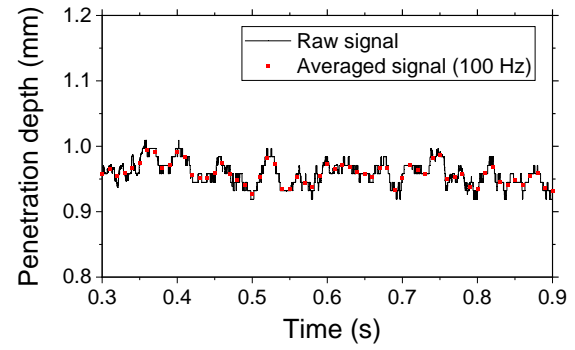
(a)



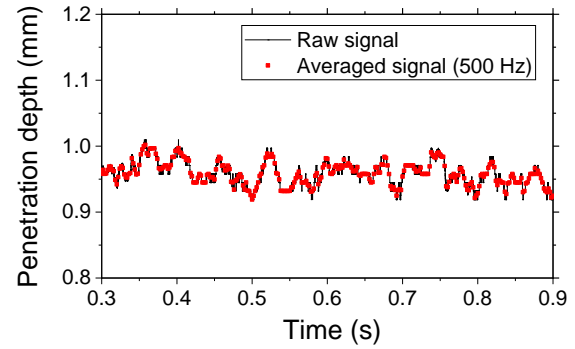
(b)

Fig. 6 Example of spectrometer signal. (a) Signal profiles for the entire wavelength and (b) for local peak wavelength.

The OCT signal sampled at 135 kHz was resampled at 100 Hz and 500 Hz by averaging every 1350 and 270 signals, respectively. As shown in Fig. 7, the down-sampled signals represented the original signals well, despite a slight attenuation of fluctuation.



(a)



(b)

Fig. 7 Raw OCT signals and resampled OCT signals at (a) 100 Hz and (b) 500 Hz

Deep learning models

Unisensor models and multisensory models were constructed to predict the weld penetration depth.

The deep learning model for unisensor models is a typical CNN model [26]. Two unisensor models were trained using sampled inputs and outputs of 100 Hz and 500 Hz. The input of the unisensor models was the CCD image of the in situ welding. A down-sampled image of 100 Hz and sampled raw image of 500 Hz were considered as input. The unisensor model comprised two blocks of convolution, batch normalization, max pooling layers, and a fully connected network (FCN) with two dense layers (Fig. 8a).

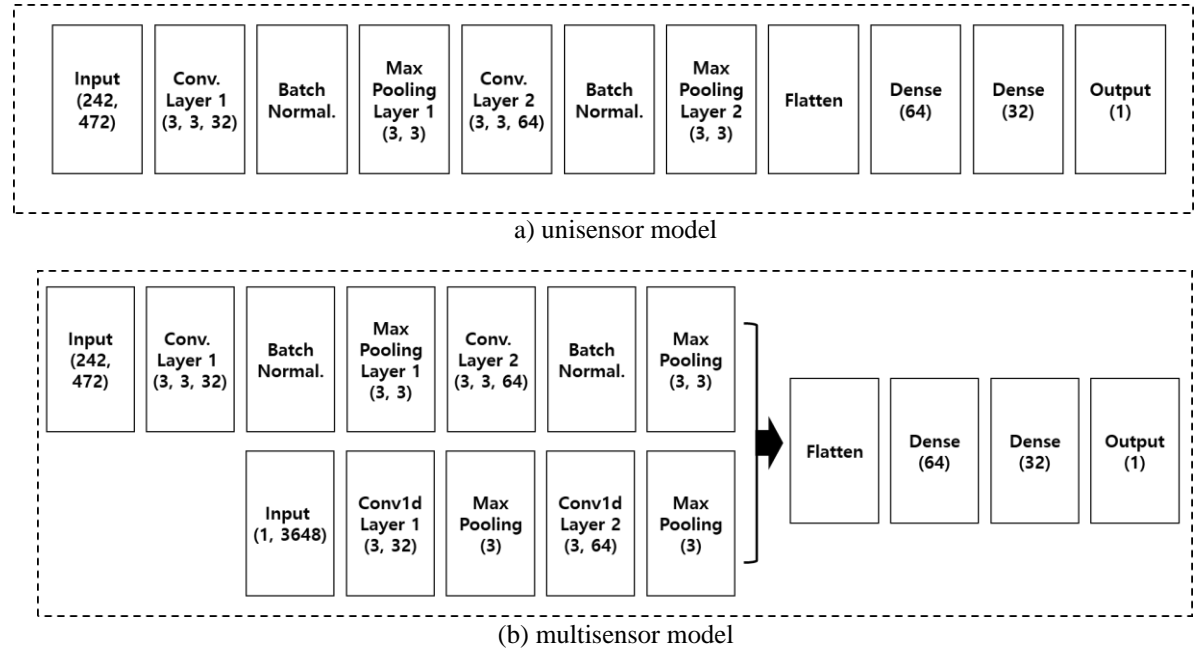


Fig. 8 Structure of deep learning models

In the multisensor models, a 2D-CNN and a 1D-CNN were concatenated, followed by an FCN (Fig. 8b). The input of the multisensor models was the CCD image and the spectrometer signal. The upper part of the multisensor model was identical to that of the unisensor model. At a particular time frame, the spectrometer signal was considered as 1-D series according to the wavelength and modeled by a 1-D CNN network. As in the unisensor models, two models with sampling frequencies of 100 Hz and 500 Hz were trained.

A rectified linear unit (ReLU) was selected as an activation function for all hidden nodes, and an identical function was used as an activation function at the output node.

Dataset and optimization method

A total of 3,000 and 15,000 data points were prepared by data acquisition and preprocessing for the 100 Hz and 500 Hz models, respectively. Data points were randomly split into training, validation, and test datasets at rates of 70%, 15%, and 15%, respectively.

The mean square error loss function and Adam optimizer were used during the training. The parameters for the Adam optimizer were learning rate = 10^{-3} , $\beta_1 = 0.9$, $\beta_2 = 0.999$, and $\epsilon = 10^{-8}$. The details of the Adam optimizer and its parameters are available in [27].

The models were trained for 1000 epochs in minibatches of 16 samples.

Results and discussion

Training and validation

The training error of the models rapidly decreased in the early stage, and continuously decreased according to the epoch. The validation error converged after a maximum of 300 epochs, indicating that the models were not overfitted. In particular, the 500 Hz models were stabilized at a significantly early epoch compared with the 100 Hz models.

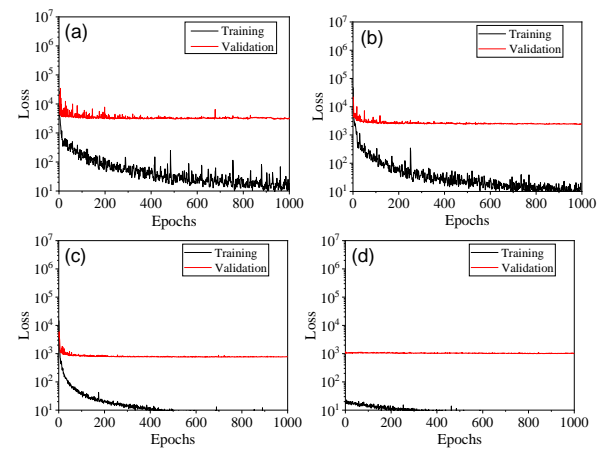


Fig. 9 Model training results for (a) 100 Hz unisensor, (b) 100 Hz multisensor, (c) 500 Hz unisensor, and (d) 500 Hz multisensor models

This is the author's peer reviewed, accepted manuscript. However, the online version of record will be different from this version once it has been copyedited and typeset.
PLEASE CITE THIS ARTICLE AS DOI: 10.2351/7.0000767

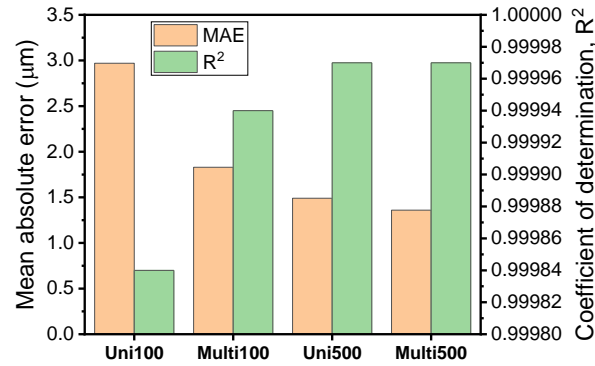


Fig. 10 Training error of 100 Hz unisensor (Uni100), 100 Hz multisensor (Multi100), 500 Hz unisensor (Uni500) and 500 Hz multisensor (Multi500) models

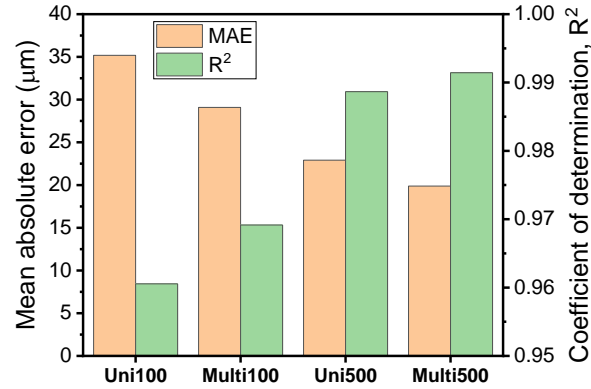


Fig. 11 Validation error of (a) 100 Hz unisensor, (2) 500 Hz multisensor, (3) 100 Hz multisensor, and (4) 500 Hz multisensor models

The mean absolute errors (MAE) in the training and validation are shown in Figs. 10 and 11. During training, all models had an MAE of less than 0.003 mm and a coefficient of determination, R^2 , of more than 0.9998. The 500 Hz models showed better prediction accuracy than the 100 Hz models, and the multisensor models were more accurate than the unisensor models. In the validation, the MAE was increased by more than ten times over the model training. As in the model training, the 500 Hz multisensor model showed the best accuracy with an MAE of 0.01988 mm and an R^2 of 0.99143.

Model test

In the model test, the trends and magnitudes of the errors were similar to those of the validation (Fig. 12). The 500 Hz multisensor model showed the best accuracy, with an MAE of 0.02035 mm and an R^2 of 0.999985. In the residual plot, the interquartile range of the 500 Hz multisensor model ranged from -0.01442 mm to 0.01648 mm; however, the maximum prediction

error was relatively high at 0.33227 mm (Fig. 13). Examination of CCD images near the maximum-residual data point revealed spattering (Fig. 14); therefore, presumably, the OCT sensor generated an inaccurate keyhole depth owing to interference of the OCT laser beam and spatter.

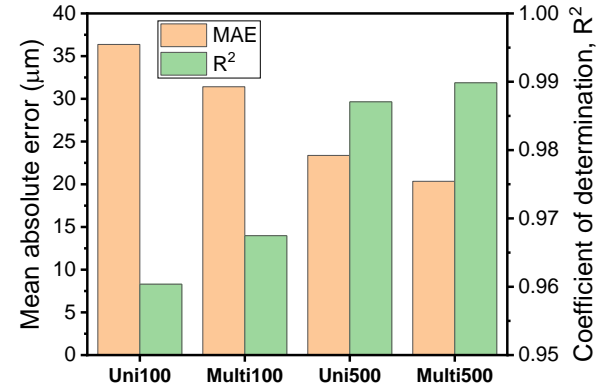


Fig. 12 Test error of 100 Hz unisensor (Uni100), 100 Hz multisensor (Multi100), 500 Hz unisensor (Uni500) and 500 Hz multisensor (Multi500) models

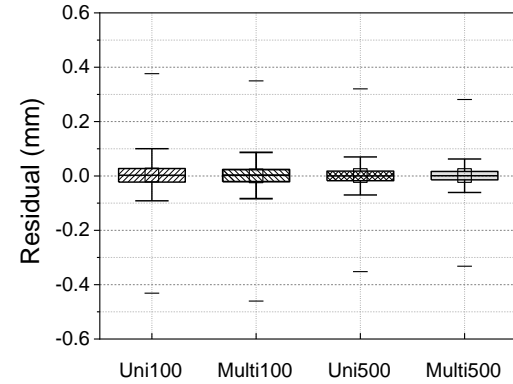


Fig. 13 Box plots of residuals of prediction using test data set

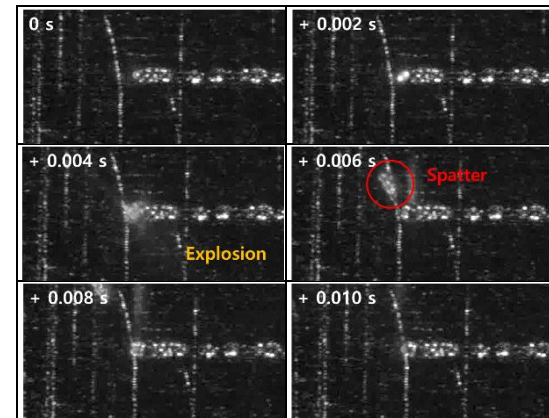


Fig. 14 CCD images near the data point with the maximum error

Verification

The trained deep learning model was verified using a welding trial with a gradually increasing laser power along the weld line. In the longitudinal section, the penetration depth was measured physically rather than using the OCT sensor (Fig. 15). The penetration depth was predicted by the 500 Hz multisensor models and then compared with the measured one (Fig. 16). The MAE for 500 Hz multisensor models was 0.02051 mm. The maximum prediction error for the 500 Hz multisensor model was 0.167 mm, which was less than 1/2 of the thickness of the upper sheet.



Fig. 15 Longitudinal cross-section of the verification experiment. The laser power increased from 600 W to 900 W, and the welding speed was 5 m/min.

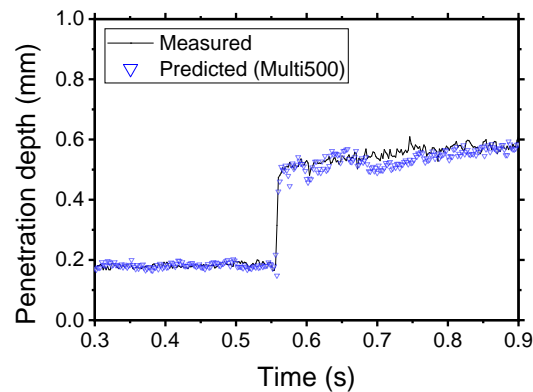


Fig. 16 Comparison of measured and predicted penetration depth in the verification experiment.

Discussion

The most accurate model in this study can predict the penetration depth, with an MAE of 0.02035 mm. As the thickness of the upper Al plate was 0.4 mm, the MAE was only 5% of the upper plate thickness. By using a high-power illumination laser, information about the laser keyhole, weld pool, and solidified weld bead was collected by the coaxial image, while only keyhole-related information was available in the laser welding of aluminum without laser illumination [16].

A higher-frequency image and auxiliary spectrometer enhance the prediction accuracy. In this study, even at the highest welding speed of 7 m/min, a sampling frequency of 500 Hz corresponds to sampling per weld

length of 0.23 mm, which reveals that the prediction system has a fairly good resolution. With advances in imaging and computing systems, a low-cost CCD and general-purpose processing system can implement 500 Hz image grabbing and penetration prediction using deep learning models.

The spectrometer signal included: material emission and reflections from the process, OCT coherence, and illumination lasers. In dissimilar metal welding, the material emission spectrum can be a good measure of the penetration into the lower metal plate. Owing to the high laser reflectivity of Al and Cu, the reflection of the process laser determines the efficiency of the laser absorption to the base metals. The spectrometer signal is inherently sophisticated and relative, and has been utilized in the qualitative sensing of welding quality. However, it can be adopted as an auxiliary sensor to improve the accuracy of the quantitative prediction of the penetration depth. As the spectrometer signals in the 500 Hz multisensor model were digitally resampled from the 100 Hz raw signals, higher frequency sampling could enhance the accuracy of the multisensor model. The current system had a relative slow sampling rate, quality classification by section is recommended rather than point by point.

OCT sensors have recently shown good performance in measuring laser keyhole depths. Laser keyholes are inherently unstable in terms of size and aperture openings. Because the OCT sensor in this study had a high sampling rate of 135 kHz, the instability could be mitigated by signal averaging, and the OCT output signal was utilized as an in situ estimate of the penetration depth. Inexpensive in-situ penetration depth measurements were possible with OCT sensors without laborious destructive testing and expensive real time X-ray systems.

Although the deep learning models showed excellent performance in most cases, spattering interfered with the OCT signal, resulting in relatively high residual outliers in the model test. In the verification test, the actual penetration depth was measured rather than being estimated from the OCT signal. The MAE was slightly higher but the maximum prediction error was smaller than that of the model test result in the previous section. The slightly higher MAE would be originated by both the uncertainties of the depth estimation model of the OCT signal and the penetration depth model trained in this study.

Conclusion

In this study, CNN models were developed to predict the penetration depth in Al/Cu laser overlap welding. The CCD images and spectrometer signals were implemented as input data, and the OCT signal was collected as the output. The penetration depth was effectively predicted with a resampled dataset of the unisensor and multisensors.

The following conclusions were drawn from this study:

1. The models based on CNN images and spectrometer signals were evaluated and compared. All models presented excellent accuracy in the test results, providing an MAE of less than 0.04272 mm and an R^2 of 0.96037.
2. The multisensor model with a high frequency (500 Hz) showed a higher estimation accuracy of an MAE of 0.02035 mm and an R^2 of 0.98985 compared with that of the low-frequency and unisensor models (100 Hz).
3. The CNN model using an OCT sensor was verified by comparing it with the actual penetration depth of a longitudinally sectioned specimen. The OCT system installation will allow the estimation of real-time penetration depth during Al/Cu welding.

Acknowledgements

We acknowledge financial and technical support provided by the Korea Institute of Industrial Technology (EH-22-060). Also, we are pleased to acknowledge support from the National Research Foundation of Korea (NRF) funded by the Korea government (MSIP) (Grant No. 2021R1A2C3010731).

References

- [1] Lee, S. S., Kim, T. H., Hu, S. J., Cai, W. W. & Abell, J. A. (2010) Joining technologies for automotive lithium-ion battery manufacturing: A review, In Proceedings of the ASME 2010 International Manufacturing Science and Engineering Conference, Erie, Pennsylvania, USA, 541-549.
- [2] Kang, M., Park, T., Kim, C. & Kim, J. (2013) Laser Welding characteristics of aluminum and copper Sheets for Lithium-ion Batteries, Journal of the Korean Welding and Joining Society 31(6), 58-64.
- [3] Solchenbach, T., Plapper, P. & Cai, W. (2014) Electrical performance of laser braze-welded aluminum-copper interconnects, Journal of Manufacturing Processes 16(2), 183-189.

[4] Das, A., Li, D., Williams, D. & Greenwood, D. (2018) Joining technologies for automotive battery systems manufacturing, World Electric Vehicle Journal 9(2), 22.

[5] M. Kang, W. Choi & Kang, S. (2019) Ultrasonic and laser welding technologies on Al/Cu dissimilar materials for the lithium-ion battery cell or module Manufacturing, Journal of Welding and Joining 37(2), 52-59.

[6] Lee, S. S., Kim, T. H., Hu, S. J., Cai, W. W., Abell, J. A. & Li, J. (2013) Characterization of joint quality in ultrasonic welding of battery tabs, Journal of Manufacturing Science and Engineering 135(2), 021004.

[7] Lee, S. S., Kim, T. H., Hu, S. J., Cai, W. W. & Abell, J. A. (2015) Analysis of weld formation in multilayer ultrasonic metal welding using high-speed images, Journal of Manufacturing Science and Engineering 137(3), 031016.

[8] Brand, M. J., Schmidt, P. A., Zaeh, M. F. & Jossen, A. (2015) Welding techniques for battery cells and resulting electrical contact resistances, Journal of Energy Storage 1, 7-14.

[9] Schmidt, P. A., Schmitz, P. & Zaeh, M. F. (2016) Laser beam welding of electrical contacts for the application in stationary energy storage devices, Journal of Laser Applications 28(2), 022423.

[10] Duh, Y.-S., Lin, K. H. & Kao, C.-S. (2018) Experimental investigation and visualization on thermal runaway of hard prismatic lithium-ion batteries used in smart phones, Journal of Thermal Analysis and Calorimetry 132(3), 1677-1692.

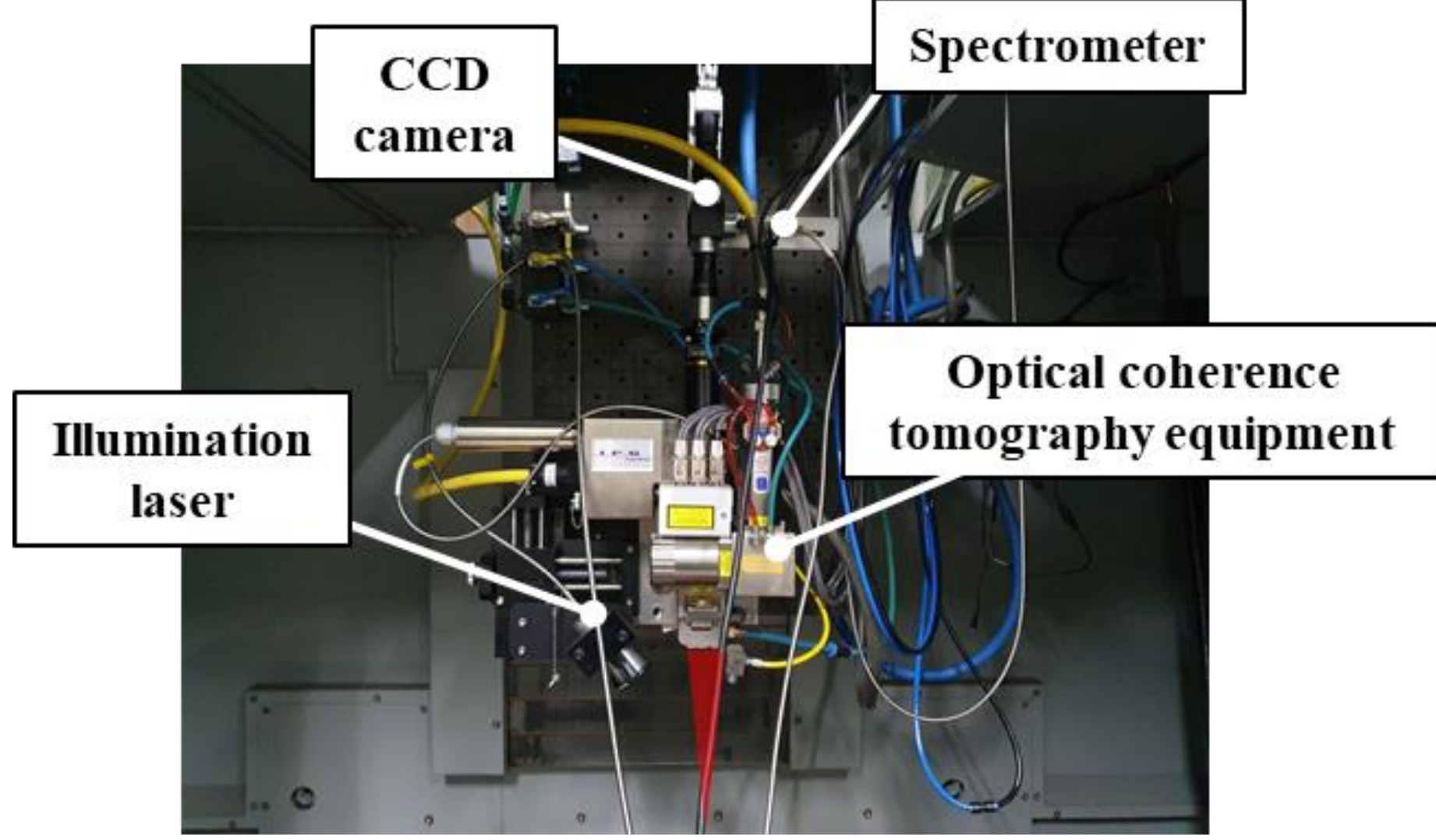
[11] Saariluoma, H., Piironen, A., Unt, A., Hakanen, J., Rautava, T. & Salminen, A. (2020) Overview of Optical Digital Measuring Challenges and Technologies in Laser Welded Components in EV Battery Module Design and Manufacturing, Batteries 6(3).

[12] Plapper, P. S., T. & Cai, W. (2013) Laser beam joining for Li-ion battery module assembly, Proceedings in the European Automotive Laser Applications, Bad Nauheim, Germany.

[13] Lee, K., Kang, S., Kang, M., Yi, S., Hyun, S. & Kim, C. (2021) Modeling of laser welds using machine learning algorithm Part I: Penetration depth for laser overlap Al/Cu dissimilar metal welds, Journal of Welding and Joining 39(1), 27-35.

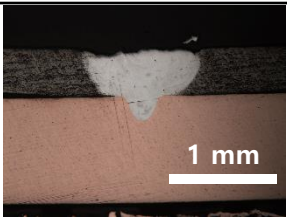
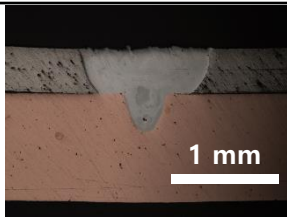
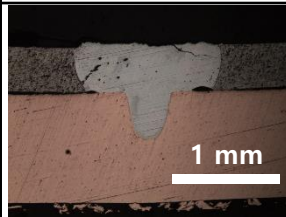
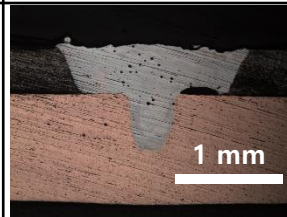
- [14] You, H., Kang, S., Kang, M. Y., S., Hyun, S. & Kim, C. (2021) Modeling of laser welds using machine learning algorithm Part II: Geometry and mechanical behaviors of laser overlap welded high strength steel sheets, *Journal of Welding and Joining* 39(1), 36-44.
- [15] Algehyne, E. A., Saeed, T., Ibrahim, M., Berrouk, A. S. & Chu, Y.-M. (2021) Investigation of dissimilar laser welding of stainless steel 304 and copper using the artificial neural network model, *Journal of Laser Applications* 33(2).
- [16] Kim, C.-H. & Ahn, D.-C. (2012) Coaxial monitoring of keyhole during Yb:YAG laser welding, *Optics & Laser Technology* 44(6), 1874-1880.
- [17] Seibold, M., Schrickler, K. & Bergmann, J. P. (2019) Characterization of optical spectrum in laser beam welding of dissimilar aluminum-copper joints and time-dependent correlation to process stages, *Proceedings in the International Symposium on Photonics and Education*, Jena, Germany, 111440U.
- [18] Mathivanan, K. & Plapper, P. (2019) Laser welding of dissimilar copper and aluminum sheets by shaping the laser pulses, *Procedia Manufacturing* 36, 154-162.
- [19] Lee, K., Kang, S., Kang, M., Yi, S. & Kim, C. (2021) Estimation of Al/Cu laser weld penetration in photodiode signals using deep neural network classification, *Journal of Laser Applications* 33(4), 042009.
- [20] Mathivanan, K. & Plapper, P. (2022) Laser welding of copper to aluminum with spiral trajectory and identification of excessive aluminum melting, *Journal of Laser Applications* 34(1).
- [21] Zhang, B., Hong, K.-M. & Shin, Y. C. (2020) Deep-learning-based porosity monitoring of laser welding process, *Manufacturing Letters* 23, 62-66.
- [22] Stadter, C., Schmoeller, M., Zeitler, M., Tueretkan, V., Munzert, U. & Zaeh, M. F. (2019) Process control and quality assurance in remote laser beam welding by optical coherence tomography, *Journal of Laser Applications* 31(2), 022408.
- [23] Sokolov, M., Franciosa, P., Sun, T., Ceglarek, D., Dimatteo, V., Ascari, A., Fortunato, A. & Nagel, F. (2021) Applying optical coherence tomography for weld depth monitoring in remote laser welding of automotive battery tab connectors, *Journal of Laser Applications* 33(1), 012028.
- [24] <https://docs.scipy.org/doc/scipy/reference/generated/scipy.signal.resample.html?highlight=resample#scipy.signal.resample>, accessed on 06/18/2022.
- [25] <https://physics.nist.gov/PhysRefData/Handbook/Tables/coppertable2.htm>, accessed on 06/18/2022.
- [26] Chollet, F. (2018) *Deep Learning with Python*, Manning Publications Co.
- [27] Kingma, D. P. & Ba, J. (2014) Adam: A method for stochastic optimization, arXiv preprint arXiv:1412.6980.


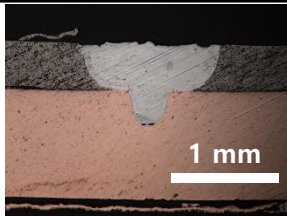
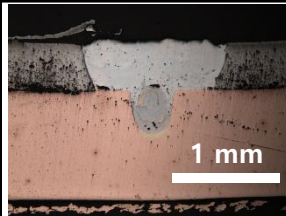
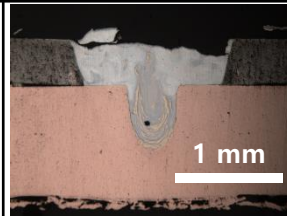
Fig. 1



This is the author's peer reviewed, accepted manuscript. However, the online version of record will be different from this version once it has been copyedited and typeset.
PLEASE CITE THIS ARTICLE AS DOI: 10.2351/17.0000767

Fig. 2

Welding speed (m/min)	3			
Laser power (W)	792	882	972	1062
Cross section				

Welding speed (m/min)	5			
Laser power (W)	877	1027	1177	1327
Cross section				

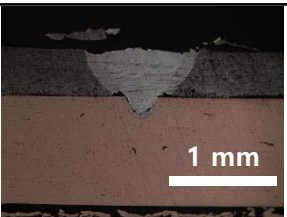
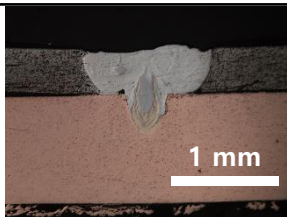

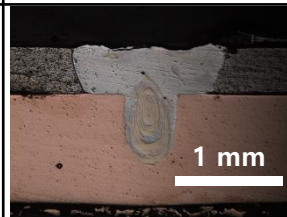
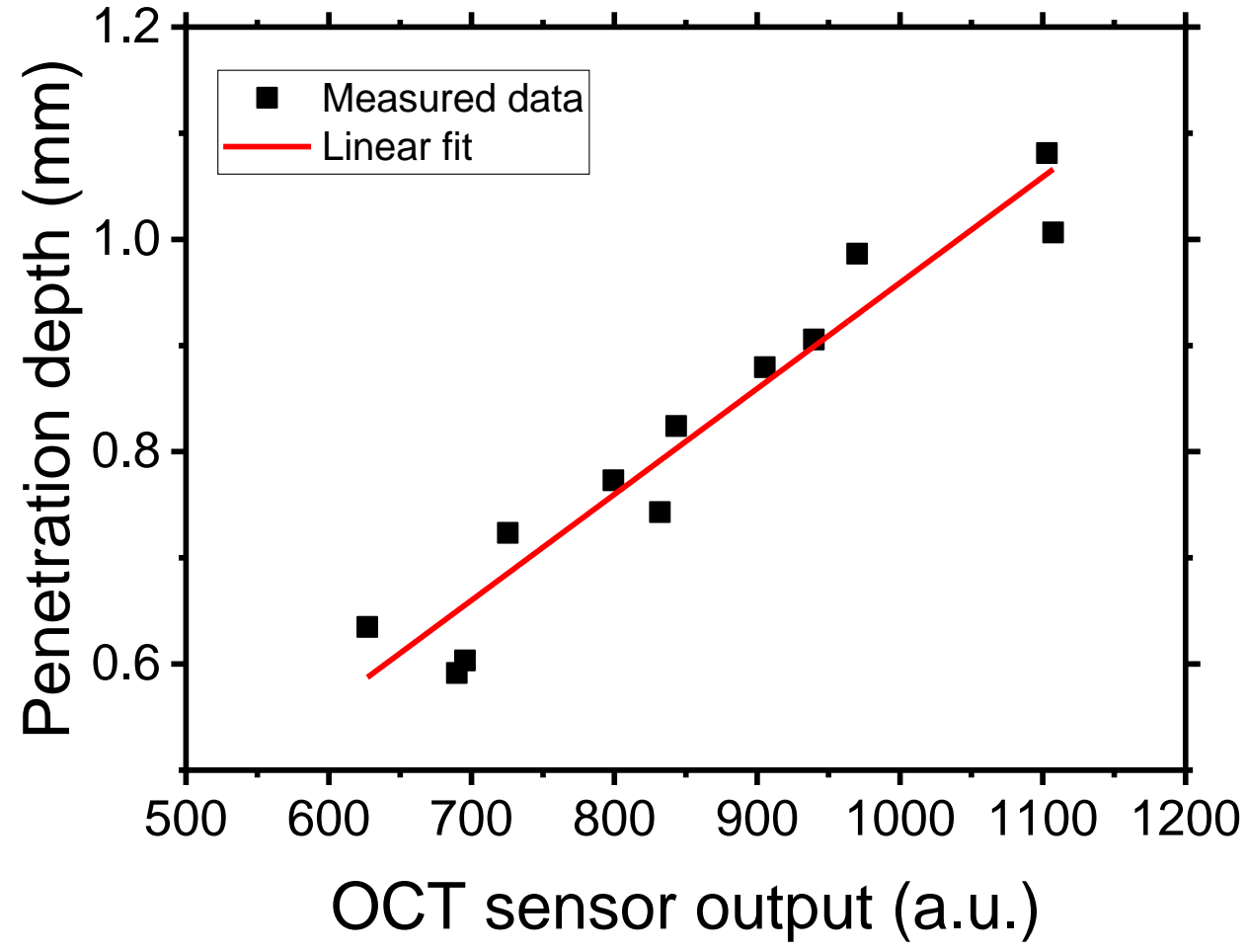
Welding speed (m/min)	7			
Laser power (W)	970	1180	1390	1600
Cross section				

Fig. 3



This is the author's peer reviewed, accepted manuscript. However, the online version of record will be different from this version once it has been copyedited and typeset.
PLEASE CITE THIS ARTICLE AS DOI: 10.2351/7.0000767

Fig. 4 image data

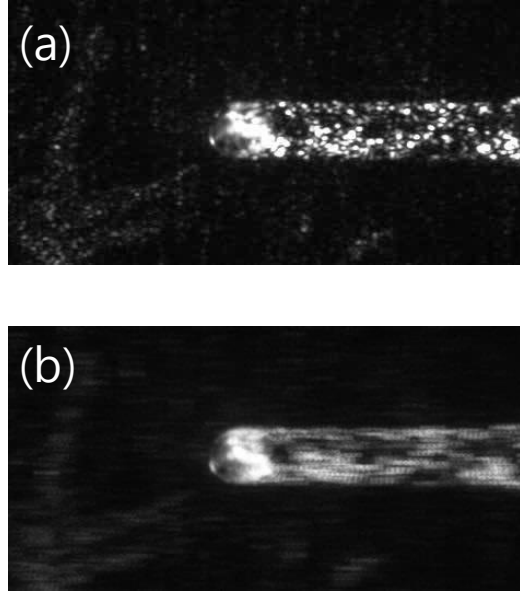
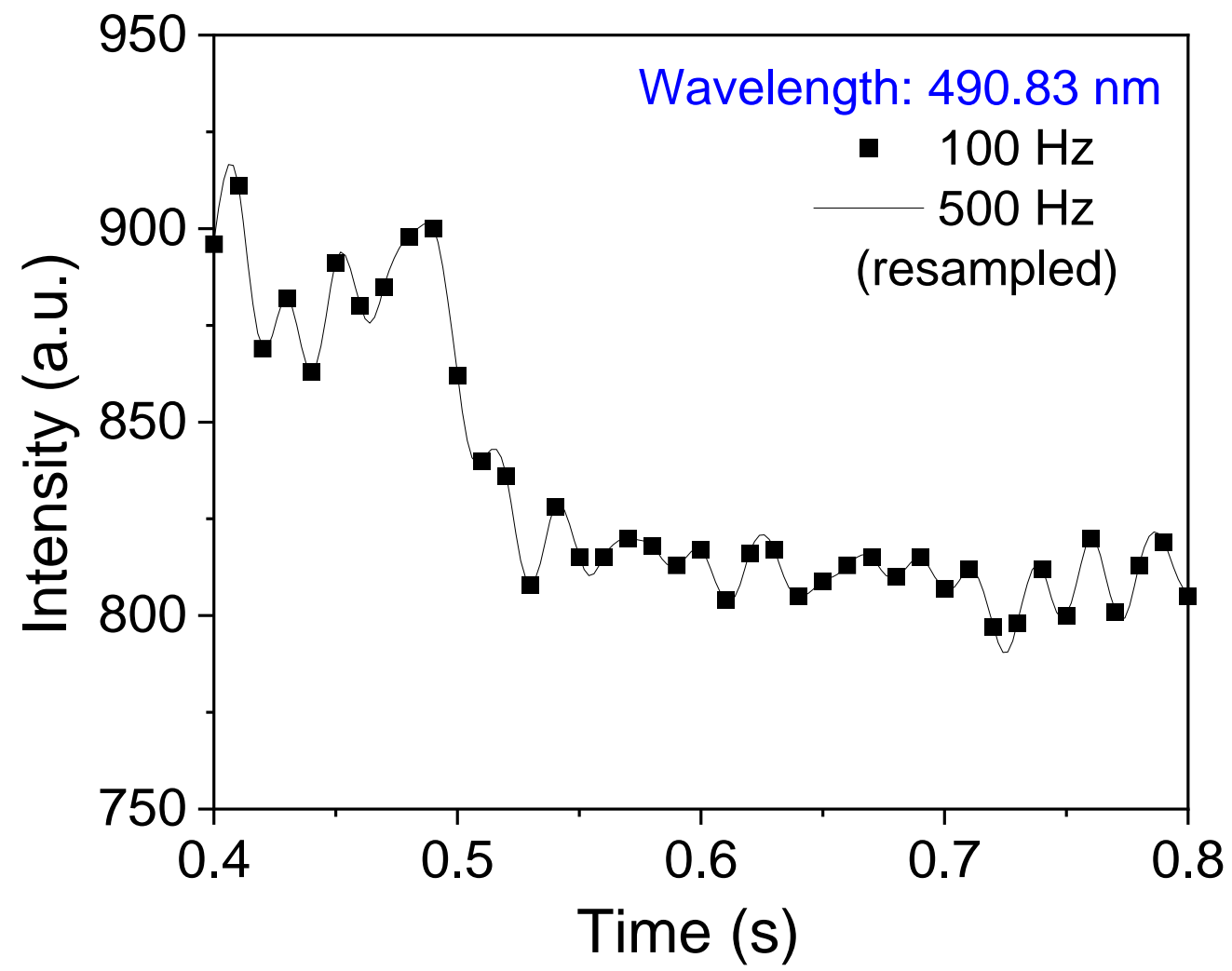


Fig. 5



This is the author's peer reviewed, accepted manuscript. However, the online version of record will be different from this version once it has been copyedited and typeset.
PLEASE CITE THIS ARTICLE AS DOI: 10.2351/7.0000767

Fig. 6a

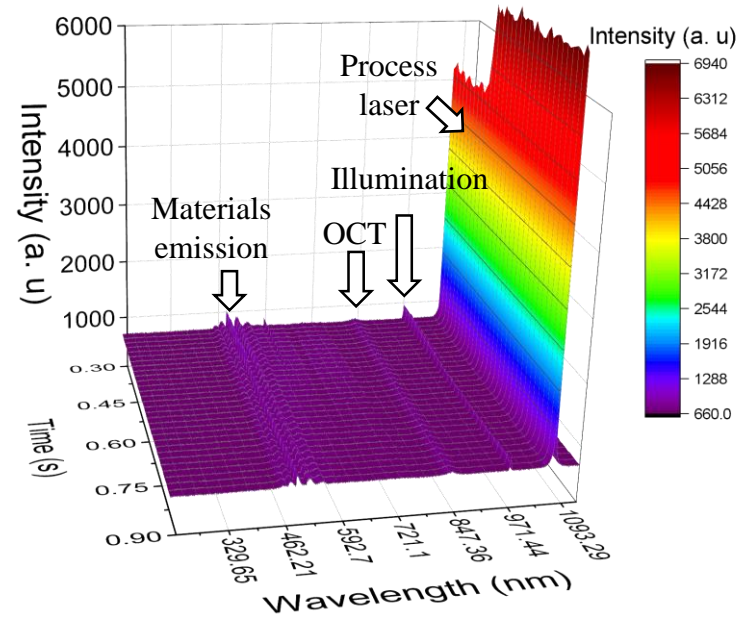


Fig. 6b

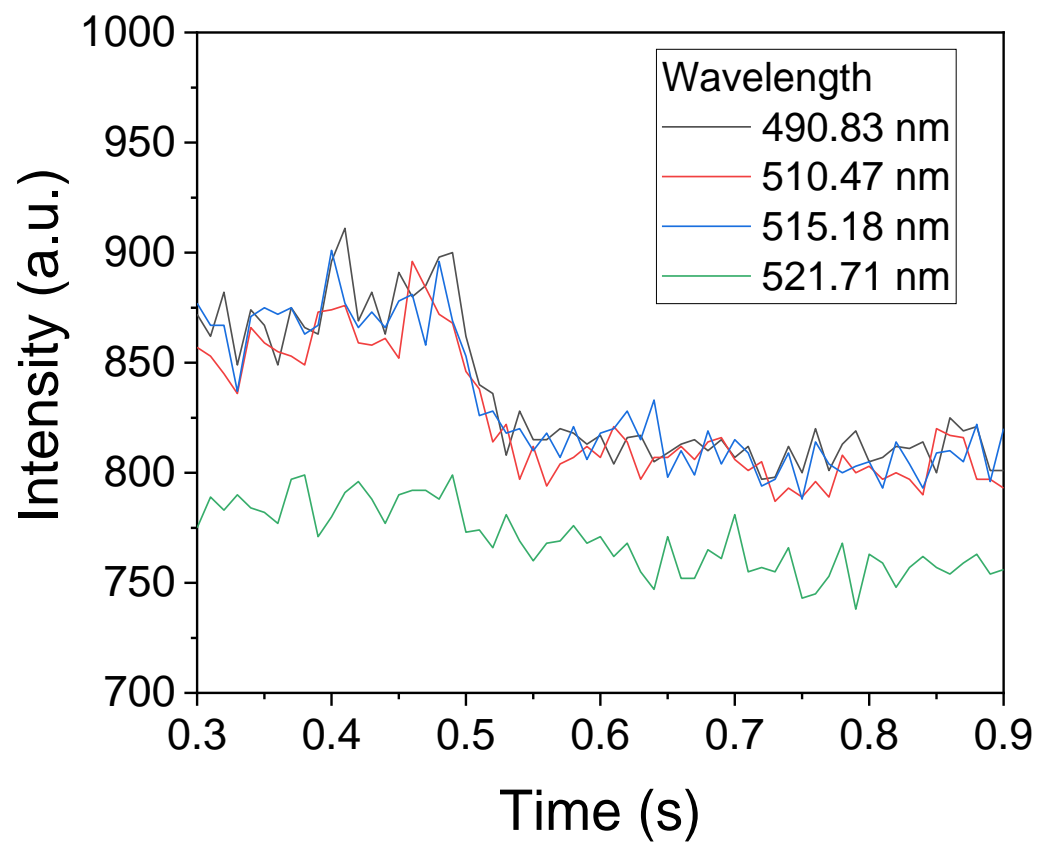


Fig. 7a

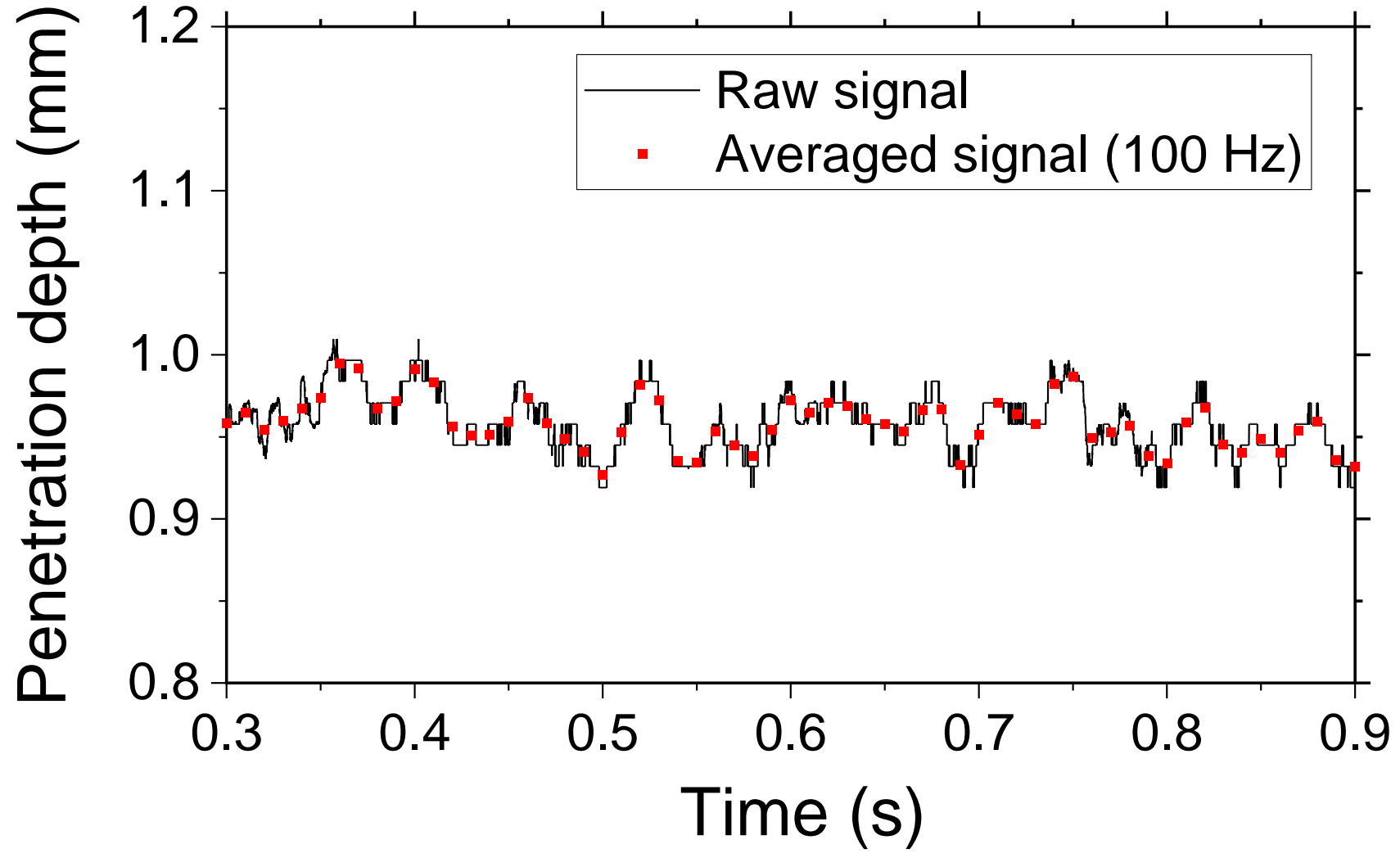


Fig. 7b

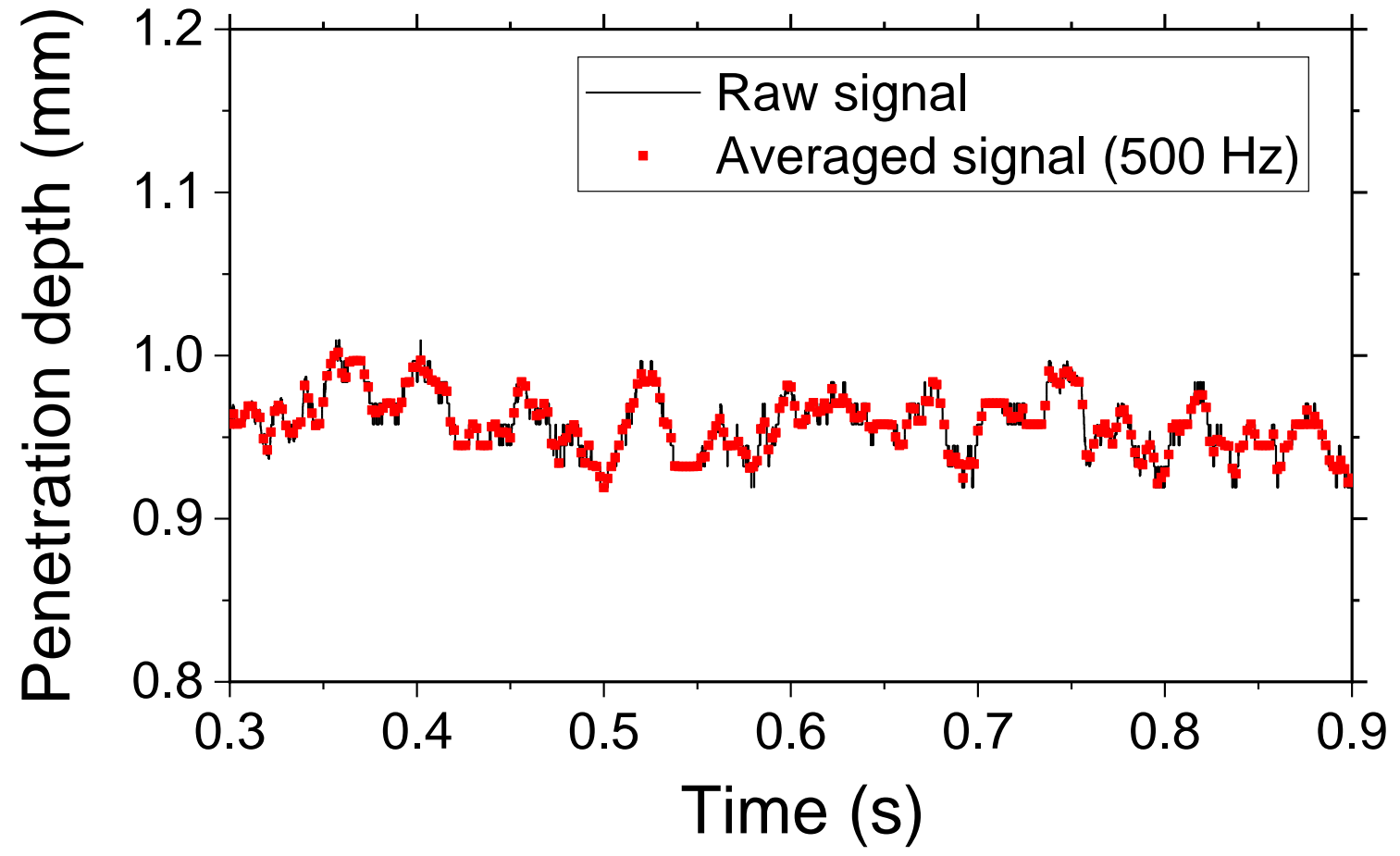
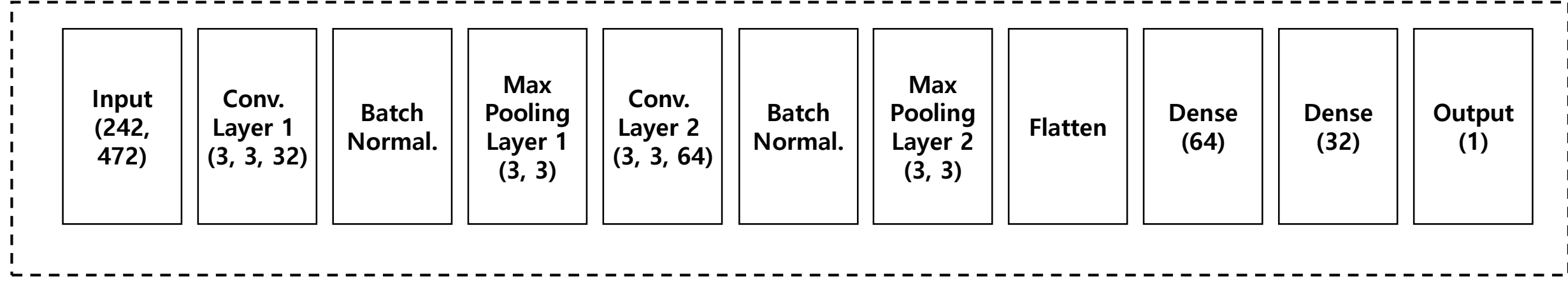


Fig. 8a

This is the author's peer reviewed, accepted manuscript. However, the online version of record will be different from this version once it has been copyedited and typeset.
PLEASE CITE THIS ARTICLE AS DOI: 10.2351/7.0000767



This is the author's peer reviewed, accepted manuscript. However, the online version of record will be different from this version once it has been copyedited and typeset.
PLEASE CITE THIS ARTICLE AS DOI: 10.2351/1.5000767

Fig. 8b

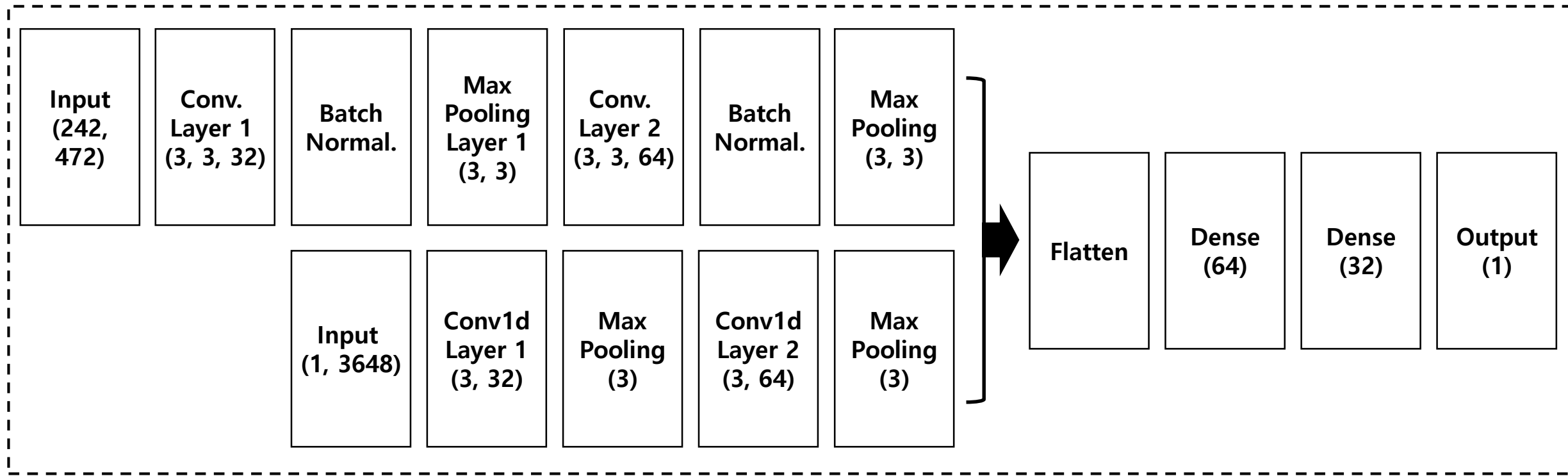


Fig. 9a

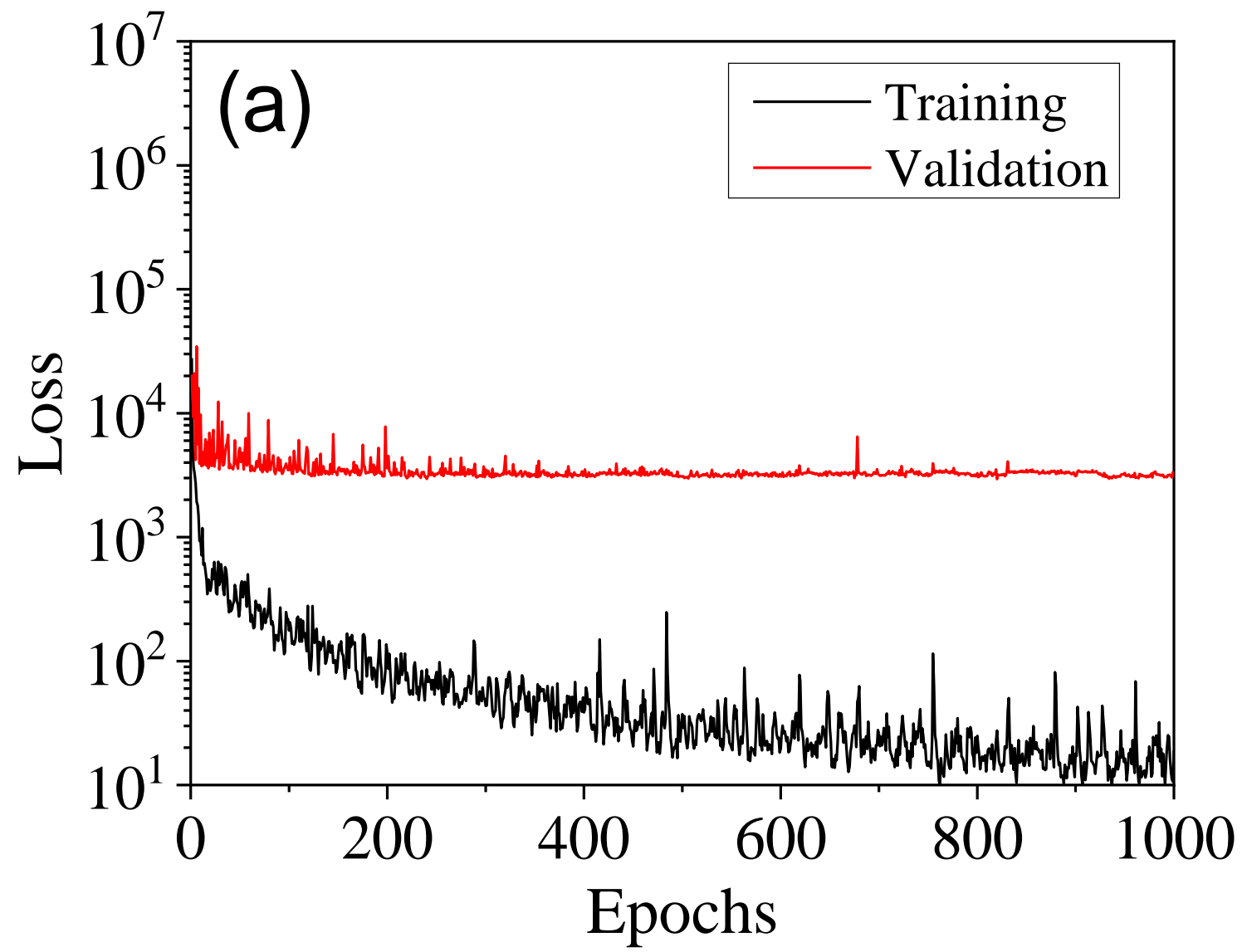


Fig. 9b

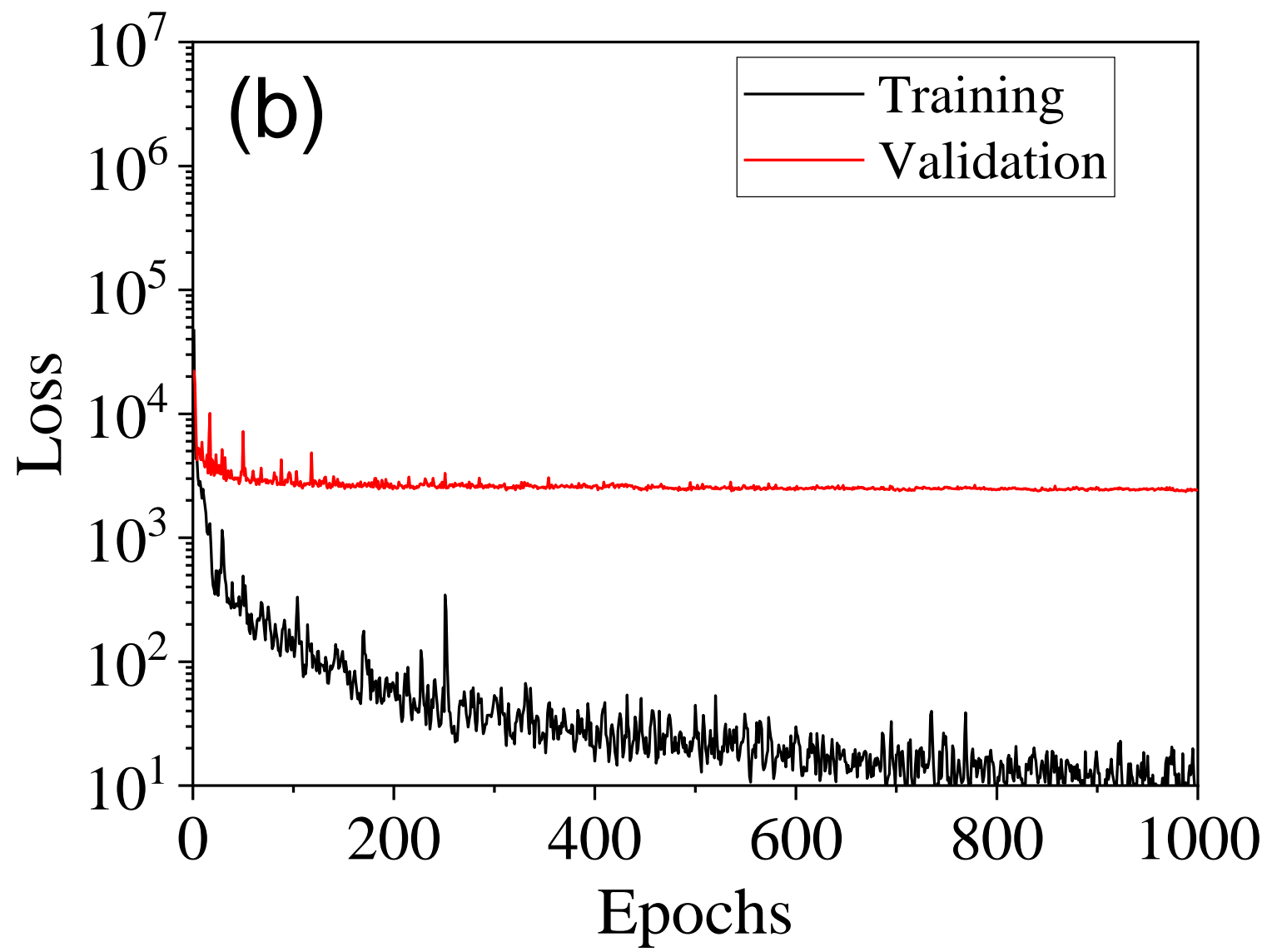


Fig. 9c

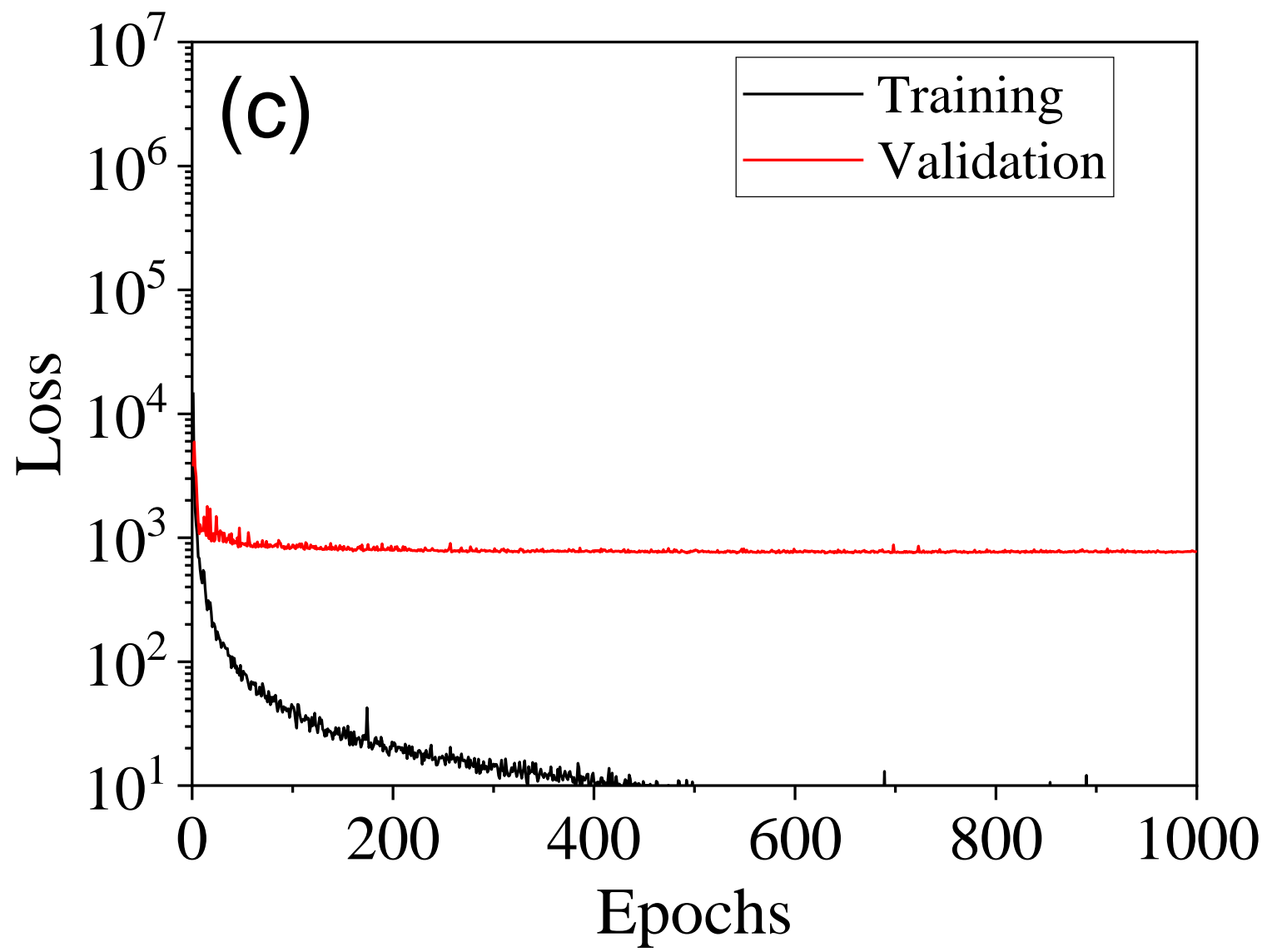


Fig. 9d

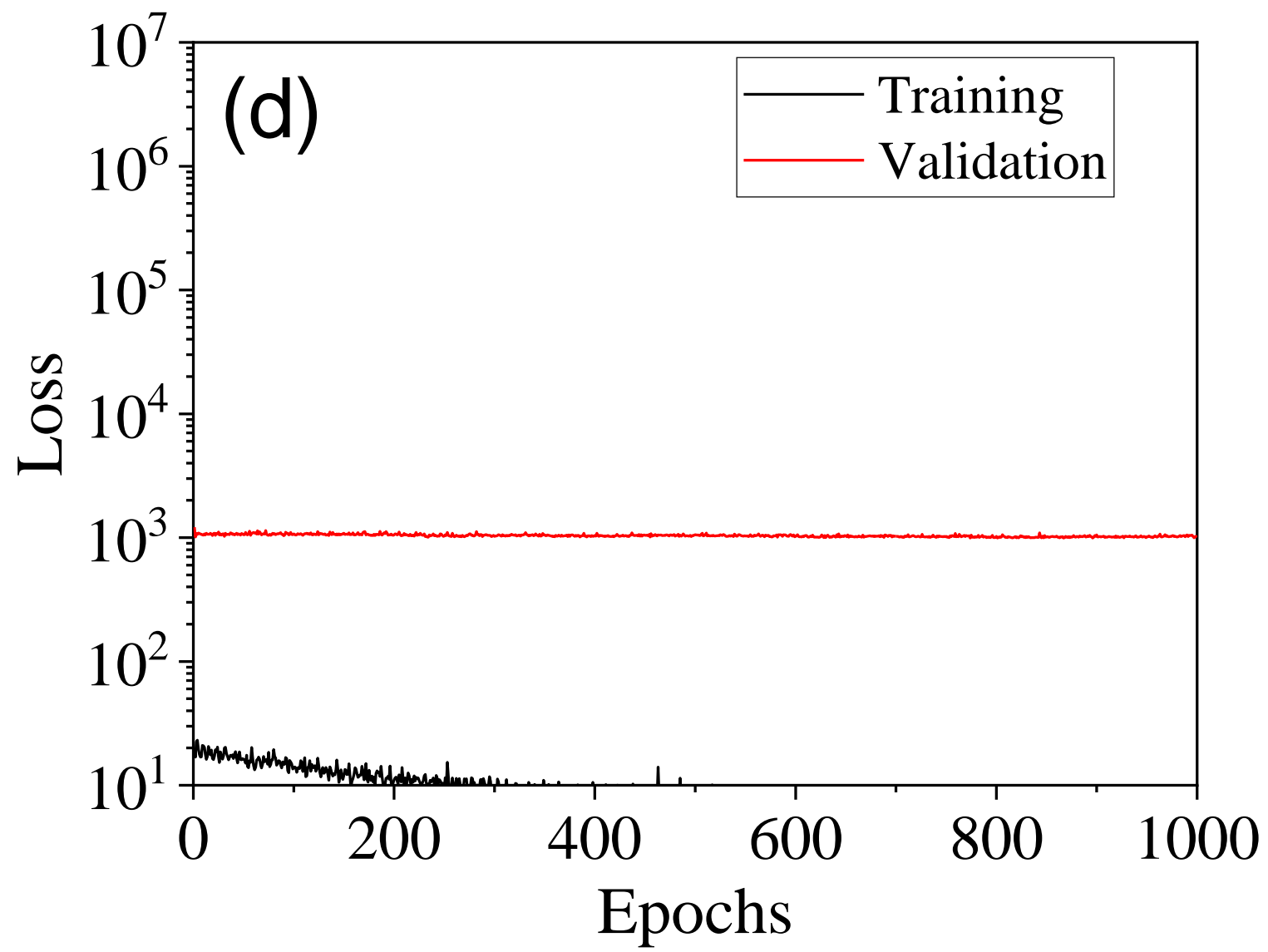


Fig. 10

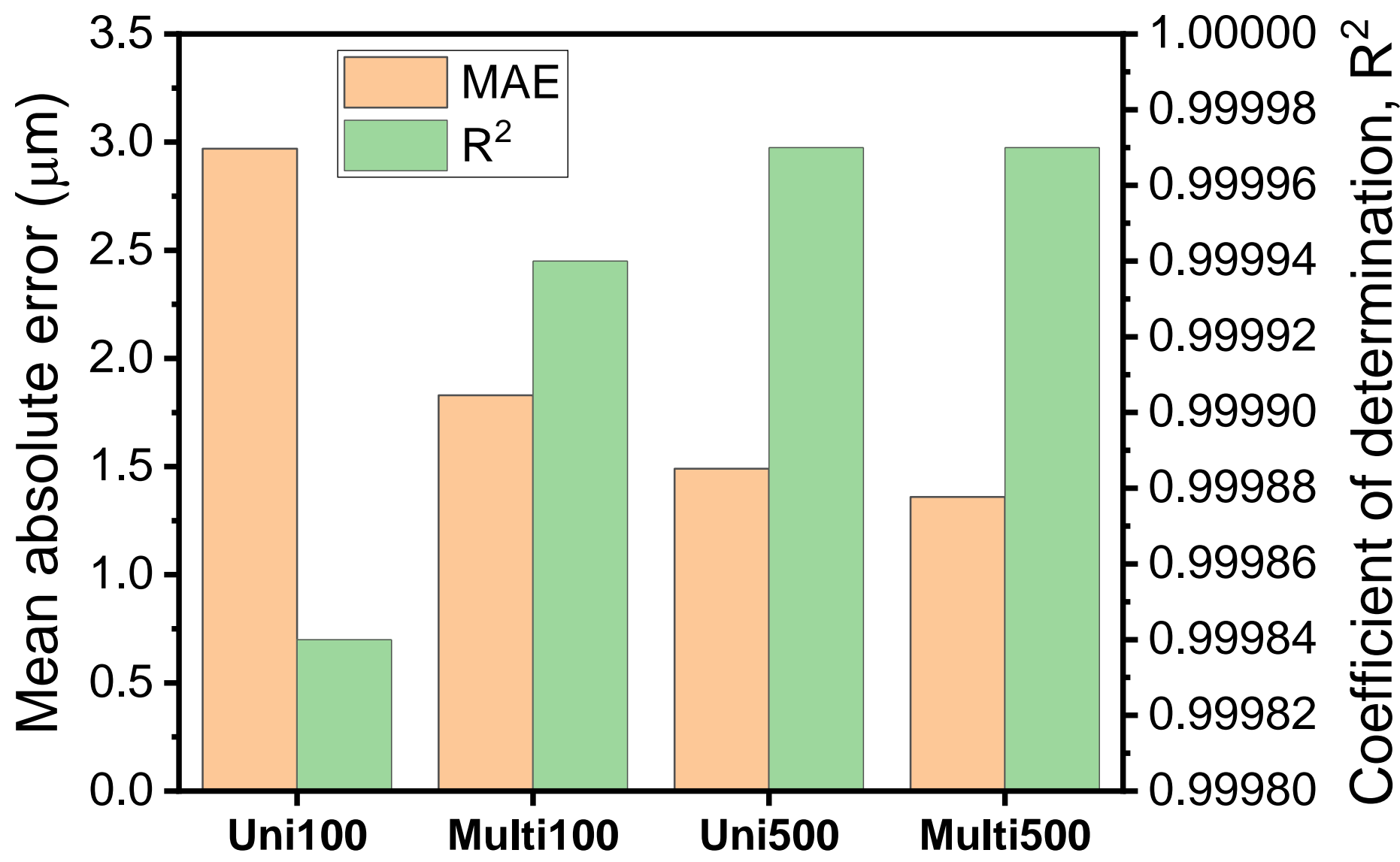


Fig. 11

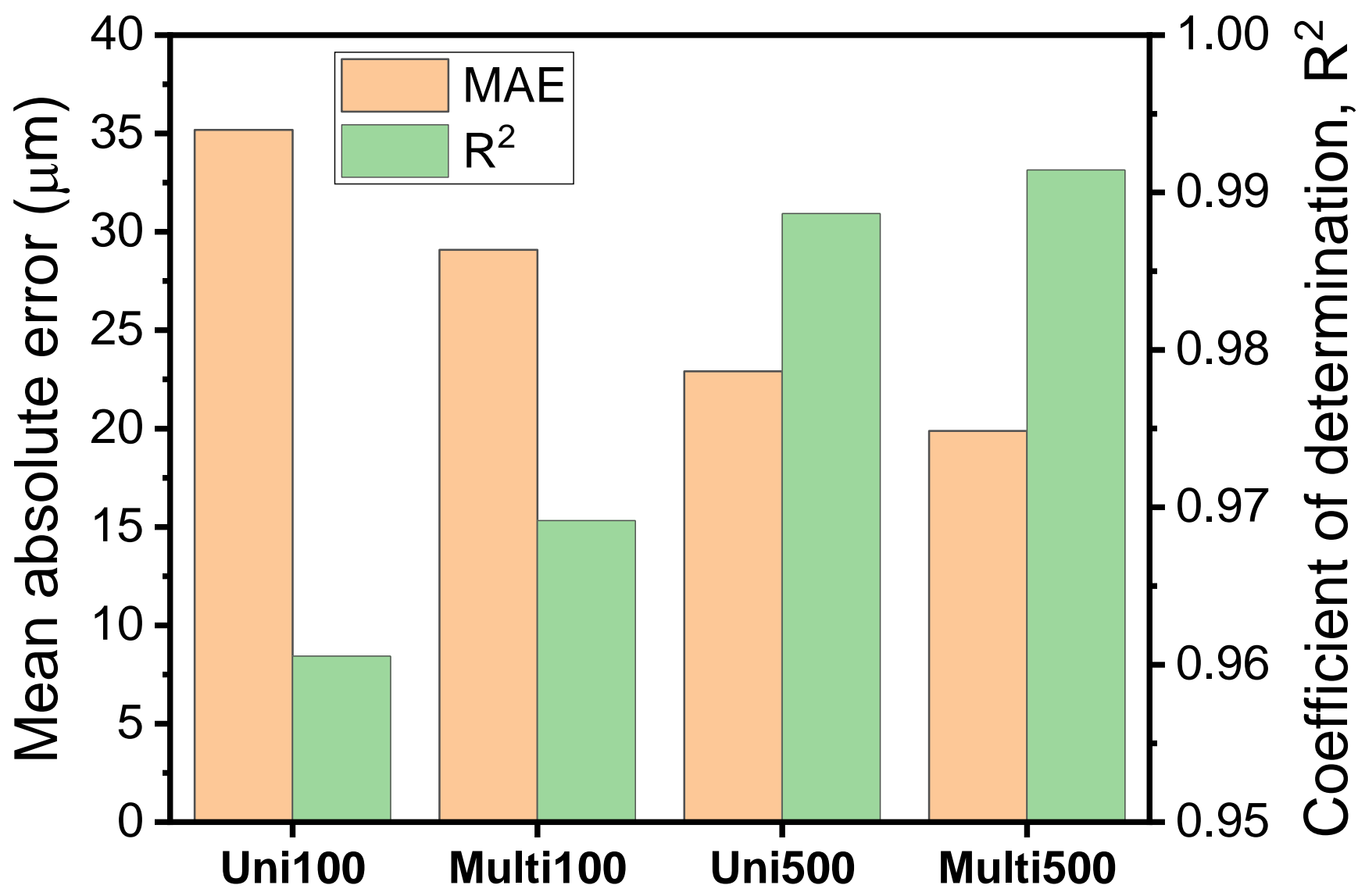


Fig. 12

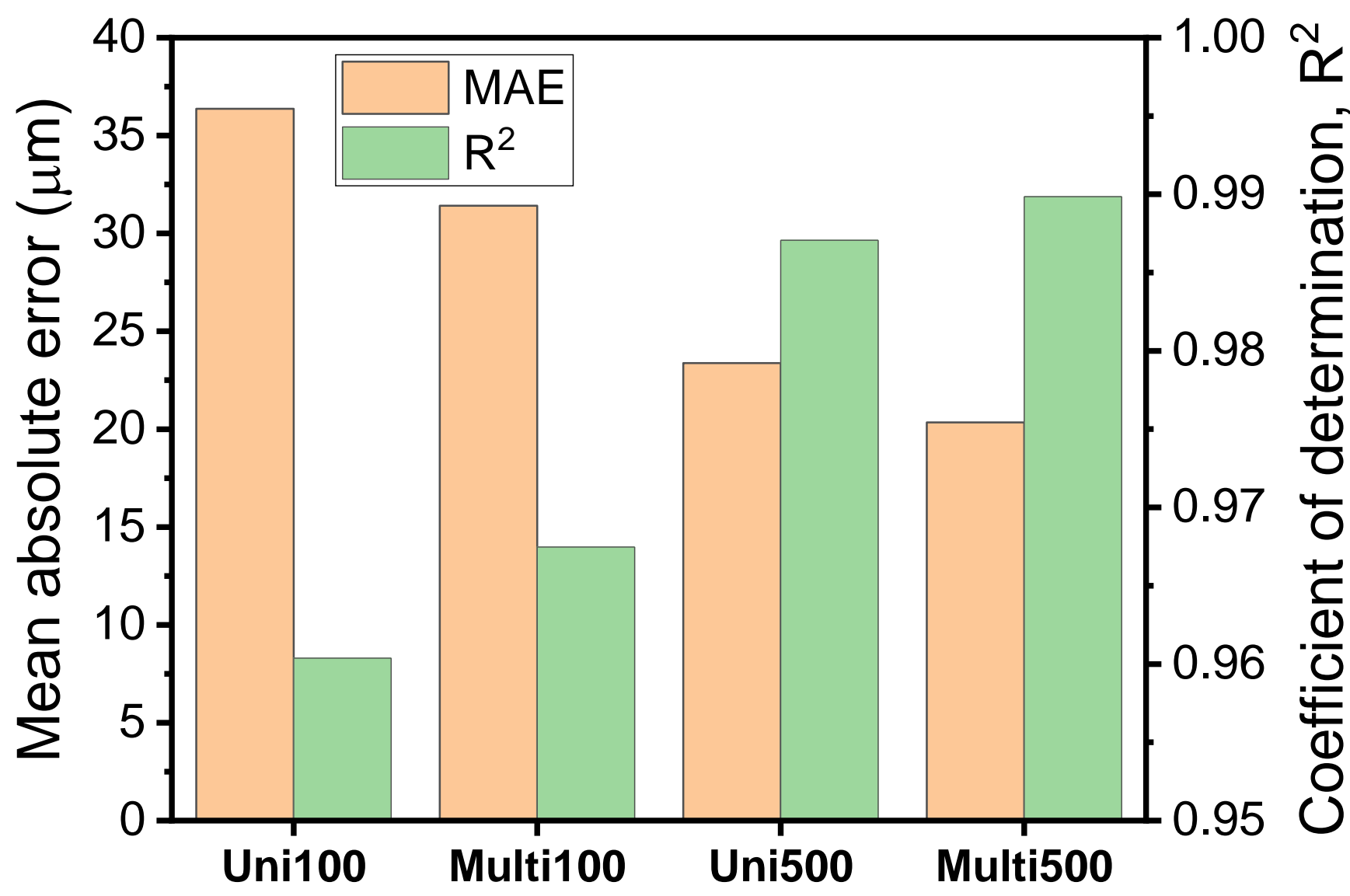


Fig. 13

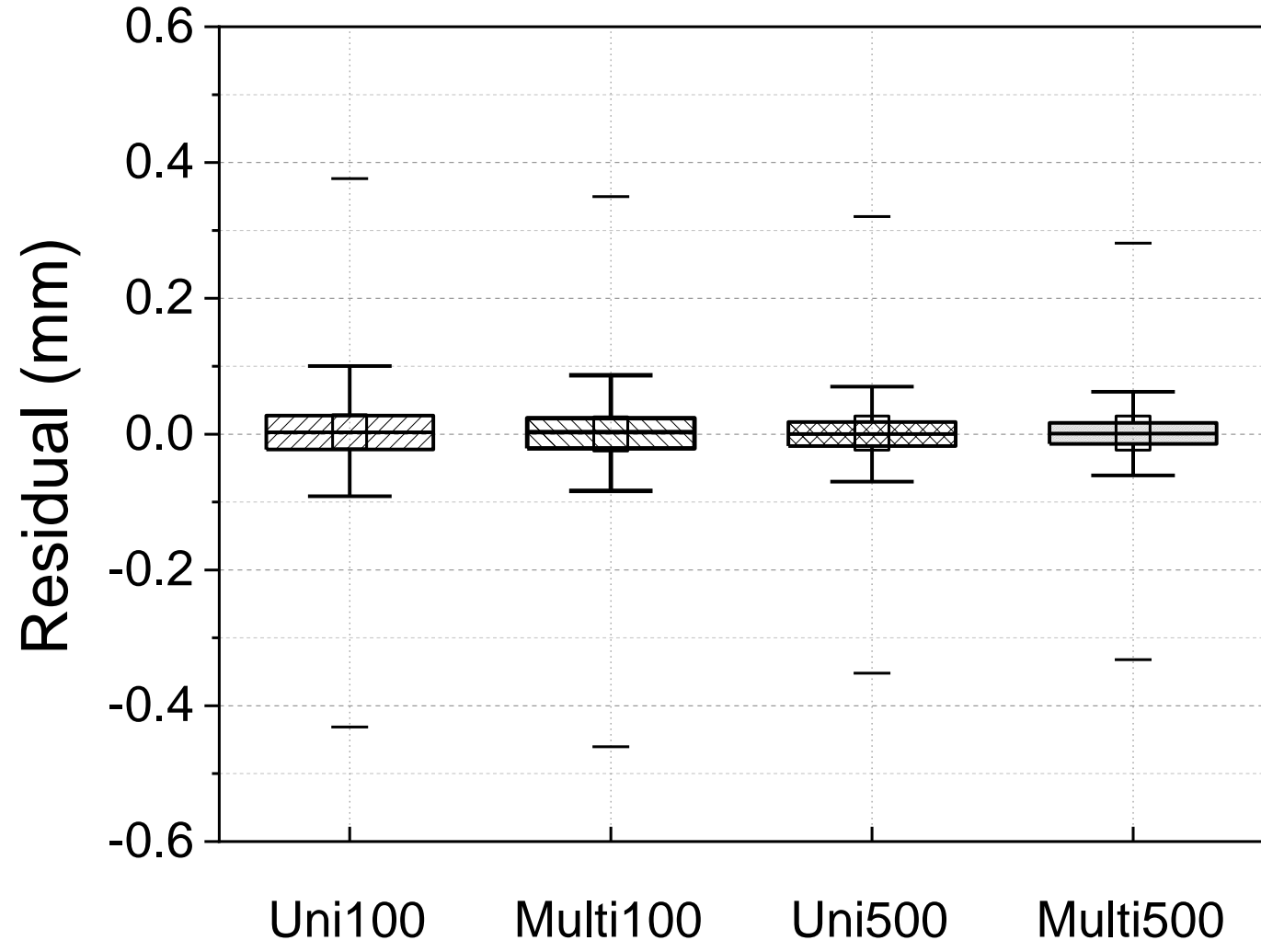
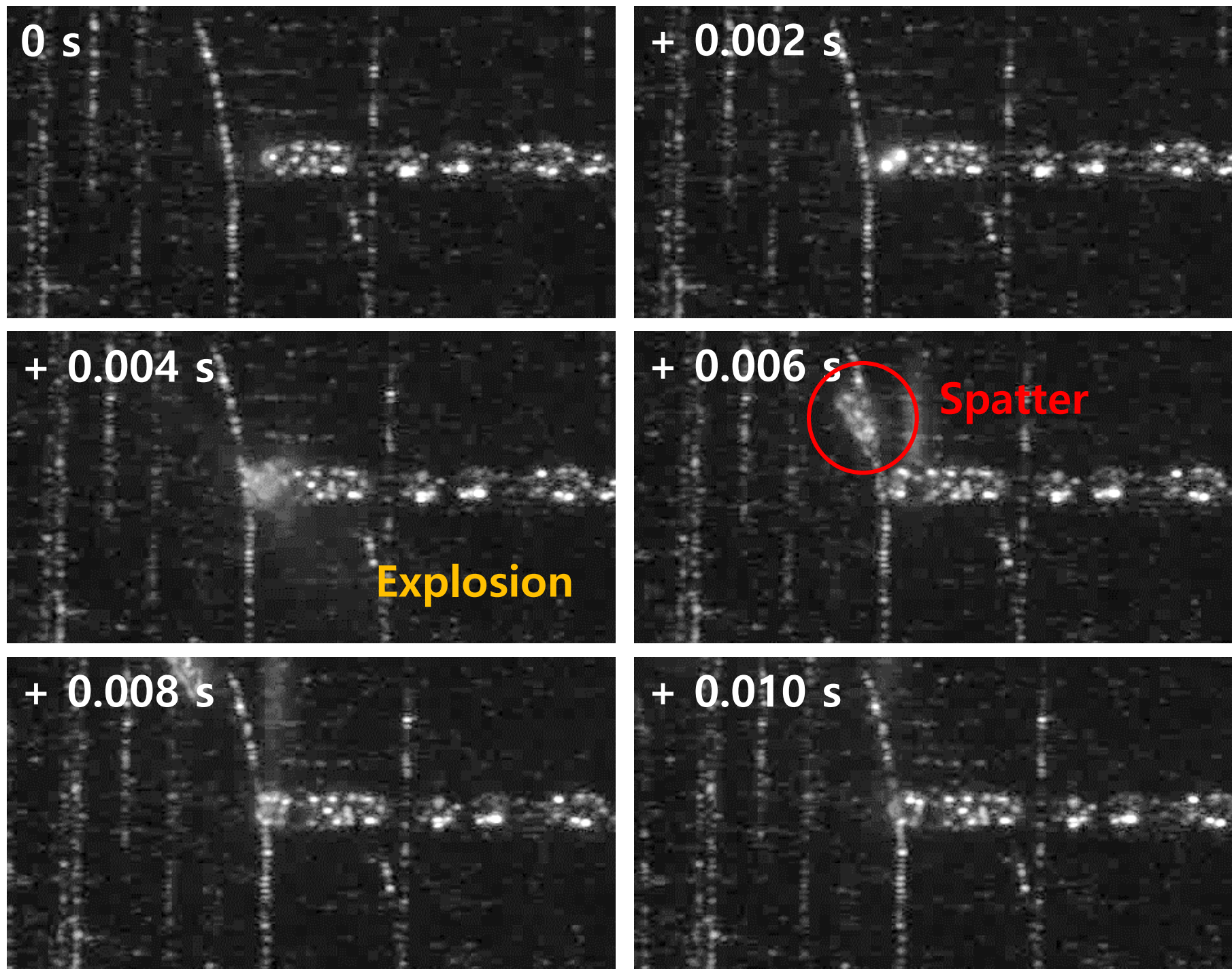


Fig. 14



This is the author's peer reviewed, accepted manuscript. However, the online version of record will be different from this version once it has been copyedited and typeset.
PLEASE CITE THIS ARTICLE AS DOI: 10.2351/7.0000767

Fig. 15

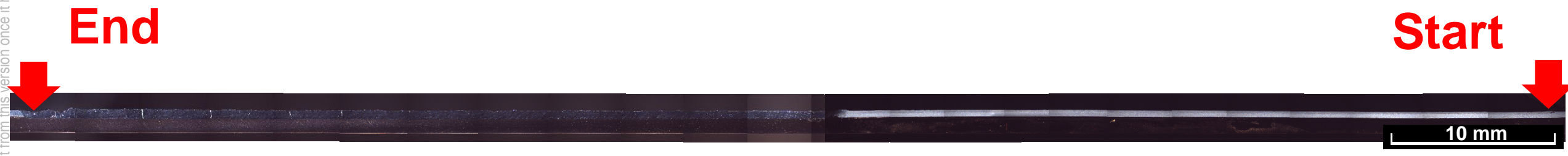


Fig. 16

